FISEVIER

Contents lists available at ScienceDirect

## Chemical Engineering Journal

journal homepage: www.elsevier.com/locate/cej



# Iron oxide supported on silicalite-1 as a multifunctional material for biomass chemical looping gasification and syngas upgrading



Xin Li<sup>a</sup>, Lijun Wang<sup>a,b,\*</sup>, Bo Zhang<sup>a</sup>, Afsaneh Khajeh<sup>c</sup>, Abolghasem Shahbazi<sup>a,b</sup>

- a Department of Natural Resources and Environmental Design, North Carolina Agricultural and Technical State University, Greensboro, NC, USA
- b Department of Chemical, Biological and Bioengineering, North Carolina Agricultural and Technical State University, Greensboro, NC, USA
- <sup>c</sup> Nanoengineering Department, North Carolina Agricultural and Technical State University, Greensboro, NC, USA

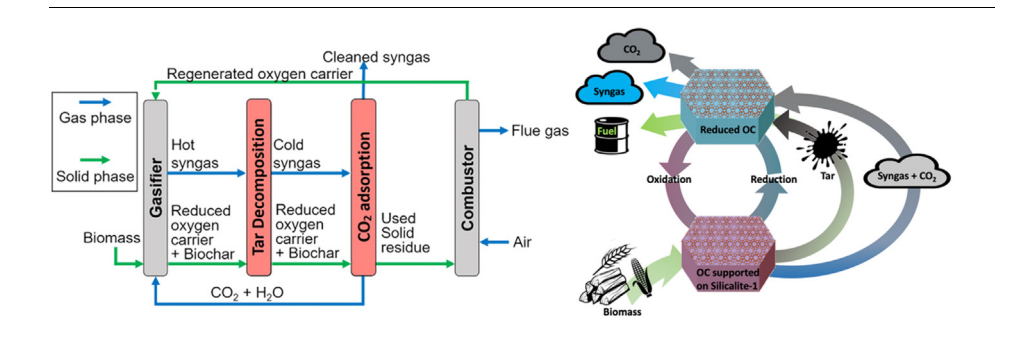
#### HIGHLIGHTS

- Iron oxide supported on silicalite-1 served as oxygen carrier to partially oxidize biomass for syngas.
- Reduced oxygen carrier exhibited outstanding tar catalytic cracking performance and high CO<sub>2</sub> adsorption capacity.
- The silicalite-1 support was resistant to undesired compound formation at high temperature.
- The novel material is suitable for cyclic process with high thermal and chemical stability.

#### ARTICLE INFO

Keywords: Chemical looping Oxygen carrier Gasification Silicalite-1 Adsorption

#### GRAPHICAL ABSTRACT



## ABSTRACT

Iron oxide supported on silicatite-1 was synthesized as a novel oxygen carrier for biomass chemical looping gasification (BCLG) with additional functionalities of its reduced form as a catalyst for tar decomposition and an adsorbent for capturing CO<sub>2</sub> in syngas. The temperature-programmed-reduction/oxidation profiles showed that the iron oxide supported on silicatite-1 had lower reduction and oxidation temperatures than the iron oxide supported on conventional silica. It was found the iron oxide supported on silicatite-1 was resistant to the formation of strong metal-support interaction and irreversible silicate in the temperature range of 650-1000 °C and exhibited high thermal/chemical stability in a cyclic process. The experimental results showed that at 900 °C, the temperature which maximize the gaseous products, the syngas contained only 0.6% C<sub>1</sub>-C<sub>4</sub> hydrocarbons/oxygenates, 3.5% one-ring aromatics, 5.7% heavier hydrocarbons/oxygenates, and 13.2% steam, meanwhile the overall selectivity towards CO2 and CO was 77.0%. The cracking conversion of toluene over the 15Fe/S-1 was 34.8% at 700 °C. The iron supported on siliclaite-1 had a better catalytic activity in tar decomposition than the iron on a conventional silica support as the silicalite-1 had higher surface area and showed better metal dispersion. As an adsorbent for CO2 capture, the reduced oxygen carrier with 15% Fe had a 1.01 mmol/g CO<sub>2</sub> adsorption capacity at 30 °C under 1 bar, which is comparable to other CO<sub>2</sub> adsorbents reported in literature. Therefore, the iron oxide supported on silicatite-1 is an effective looping material as an oxygen carrier for biomass gasification, a catalyst for tar decomposition and an adsorbent for CO2 capture.

E-mail address: lwang@ncat.edu (L. Wang).

<sup>\*</sup> Corresponding author.

#### 1. Introduction

Biomass gasification is a process in which a solid carbonaceous material is partially oxidized to produce a gas mixture of syngas mainly including carbon monoxide and hydrogen [1]. The syngas can be used to produce a variety of chemical products, such as methanol and other hydrocarbons [2]. However, due to the relatively low energy density and high moisture content of biomass, biomass gasification suffers from low efficiency and high cost, compared with gasification of other fossil fuels such as coal [3]. The considerable amount of tar derived from biomass gasification can cause the contamination of catalysts in downstream processes [4].

The concept of chemical looping processes (CLPs) was introduced in early 1900 s and has received intensive applications since 1997 [5]. CLPs are essentially cyclic processes that are based on a set of redox reactions using looping materials (LMs) such as metal oxides. CLPs have been applied for the combustion, gasification and reforming of biomass using a metal oxide as an oxygen source, known as oxygen carrier (OC), to produce heat, electricity, fuels and chemicals [6,7]. Biomass chemical looping gasification (BCLG) has several potential advantages: 1. the heat required for the endothermic biomass gasification could be provided by circulating a high-temperature oxygen carrier from a combustor; 2. the use of lattice oxygen in a recycling oxygen carrier saves the cost for producing pure oxygen or steam that are usually used as gasifying agents; 3. the heating value of the syngas produced by BCLG is higher because lattice oxygen is more prone to partially oxidize the fuels than gaseous oxygen [8].

However, the high tar and CO<sub>2</sub> contents in the syngas produced by traditional BCLG limit its applications in downstream synthesis and lower the carbon utilization efficiency. A study showed that efficient thermal tar cracking required at least 1250 °C for 0.5 s, which is energy intensive [4]. Ni is a promising catalyst for catalytic cracking or reforming [9], but the high price of Ni is not competitive for its commercialization. Therefore, the development of inexpensive oxygen carriers which could reduce the tar content in the gasification products is essential for BCLG. The deactivation of OCs during biomass conversion also impedes its scale-up and commercialization. A study showed that the agglomeration of iron oxide supported on alumina occurred when magnetite (Fe<sub>3</sub>O<sub>4</sub>) was transformed into wüstite (FeO), resulting in the deactivation. The low melting point of Cu (1085 °C) leads to more serious agglomeration than iron during a thermal process [10]. Current approach to ameliorate the deactivation caused by agglomeration is mainly adding dopants into the OC for stabilizing reactivity and enhancing strength [11–13].

Fe-based OCs have low price, high mechanical strength, high melting point, good chemical stability and non-toxicity [14]. Previous studies showed that Fe-based materials exhibit acceptable reactivity for  $H_2$  and CO, with weak reactivity for  $CH_4$  [15,16]. It was also reported that metallic iron was highly active to catalyze tar decomposition in most Fe-based catalysts [17–20]. In addition, the advantages of Fe-based OCs also includes the resistance to carbon formation [10] and sulphide/sulphate formation [21]. Therefore, iron oxide with special designs and modification could be a potential OC for simultaneous BCLG and syngas upgrading. Due to its limitation in oxygen transport capacity and solid circulation rate, the content of  $Fe_2O_3$  in the OC is generally higher than 10 wt% [16].

In aspect of catalysts, traditional supports such as silica and alumina are used to prevent the agglomeration of active components and thus deactivation [22,23]. But these supports suffer from the formation of strong metal-support interaction or even irreversible compounds such as silicate and spinel at a high temperature [24,25]. Silicalite-1 is a crystalline polymorph of  $SiO_2$  with MFI zeolite framework. Like most zeolites, it has a high thermal and chemical stability owing to its crystal system. Due to its microporous structure and high surface area, silicalite-1 is broadly used in separation [26–28] and catalysis [29–31].

The objective of this study was to synthesize and characterize Fe<sub>2</sub>O<sub>3</sub>

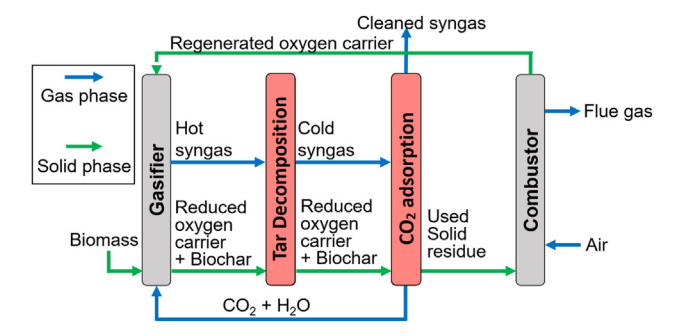


**Fig. 1.** Schematic of the upgraded chemical looping of biomass gasification (The red columns are the additional units integrated in the conventional process). (For interpretation of the references to colour in this figure legend, the reader is referred to the web version of this article.)

supported on silicalite-1 (Fe/S-1) with various loadings as multifunctional materials that can be used to improve efficiency of BCLG and the quality of the syngas. The feasibility studies of the Fe/S-1 as a multifunctional material for biomass gasification, catalytic cracking of tar, and  $\rm CO_2$  capture were performed and the results were compared with the performance of  $\rm Fe_2O_3$  supported on amorphous fumed silica (Fe/SiO<sub>2</sub>).

#### 2. Experimental section

#### 2.1. Experimental hypothesis

The hypothesis of this study is that the outstanding adsorption capacity and stability of silicalite-1 as a catalyst support can be combined with the advantages of Fe-based OC to develop a multifunctional material as an oxygen carrier at its oxidized form, and a catalyst for tar decomposition and adsorbent for  $\rm CO_2$  removal at its reduced form to be used in a novel BCLG process as shown in Fig. 1.

In the above BCLG process, biomass is partially oxidized in a gasifier by the lattice oxygen provided by the oxygen carrier, at  $500-1300\,^{\circ}\mathrm{C}$  depending on the types of the biomass. Instead of being transferred to the combustor for regeneration in conventional BCLG processes, the reduced OC that is mixed in the biochar is used as a catalyst to decompose the tar vapor present in the crude syngas with unexpected  $\mathrm{CO}_2$ . After cooling down, the solid mixture is thereafter used as an adsorbent for  $\mathrm{CO}_2$  separation from the gas phase in order to obtain a cleaner syngas with higher heating value and less contaminants for downstream process such as Fischer-Tropsch synthesis. The solid mixture is finally oxidized in air to regenerate the oxygen carrier and increase its temperature for the next cycle.

OC plays a significant role as it severs as a multifunctional material to circulate in various steps of the above BLCG process. A proper OC should have the following desirable features: 1. providing lattice oxygen for partial oxidation of biomass in its oxidized form; 2. catalytic activity in tar decomposition in its reduced form; 3. high  $\rm CO_2$  adsorption capacity in the reduced form; 4. stability in a cyclic process.

#### 2.2. Synthesis of oxygen carriers

Silicalite-1, as the support of iron oxide, was synthesized using the hydrothermal method. A total of 15.4 mL tetraethyl orthosilicate (TEOS) was mixed with 18.6 mL of 1 M tetrapropylammonium hydroxide (TPAOH) aqueous solution. Additional 30.9 mL deionized water was then added to form a slurry with a molar composition of: 1  $SiO_2:0.27$  TPAOH: 4 EtOH: 46  $H_2O$ . The slurry was vigorously stirred at a room temperature for 5 h before being transferred into a Teflonlined autoclave for crystallization at 170 °C for 72 h. The slurry was then centrifuged and washed by deionized water for 4 times and then dried at 100 °C overnight. The silicalite-1 was obtained after being

calcined in an air flow at  $550\,^{\circ}\text{C}$  for 6 h. Fumed silica that was purchased from Sigma-Aldrich as a support for comparison.

Iron oxide was loaded to the supports using the incipient-wetness impregnation (IWI) method. The capacities of water adsorption were 0.1 mL/g and 0.5 mL/g for silicalite-1 and SiO<sub>2</sub>, as measured using a titration method. In order to make oxygen carriers with intended Fe loading of 15, 20 and 25 wt%, 0.4 mL and 2 mL aqueous solutions of the desired amount of Fe(NO) $_3$ ·9H $_2$ O were added to 4 g of siliclaite-1 and SiO $_2$ , respectively. The samples were dried at 100 °C overnight and calcined in a furnace at 500 °C for 4 h.

#### 2.3. Characterization of oxygen carriers

The X-ray diffraction (XRD) analysis was carried on a D8 Discover X-ray diffractometer (Bruker Optics Inc., Billerica, USA) at 40.0 kV and 40.0 mA. Diffraction patterns were recorded using CuK $\alpha$  radiation (wavelength of 1.5406 Å) over a 20 range of 5.0°–70.0° with a step size of 0.02° and identified using the database provided by the Joint Committee on Powder Standards (JCPDS). Surface morphology and structure, energy dispersive X-ray spectroscopy, and element mapping were studied by an Auriga field emission scanning electron microscope (FESEM, Carl Zeiss AG, Oberkochen, Germany). Nitrogen adsorption—desorption isotherms were measured by a 3Flex surface characterization analyzer (Micromeritics Instrument Corp., Norcross, USA) at  $-196~^{\circ}$ C. Prior to the analysis, all samples were degassed at 300 °C for 8 h. The total surface area and external surface area were calculated using the Brunauer-Emmett-Teller (BET) equation and t-plot method, respectively.

#### 2.4. Redox reaction of oxygen carriers

The redox behavior of the oxygen carriers was investigated with the temperature programmed reduction (TPR) and subsequent temperature programmed oxidation (TPO) methods in an AutoChem 2920 analyzer (Micromeritics Instrument Corp., Norcross, USA). The samples were activated in an inert He gas flow at 300 °C for 2 h prior to analysis. After cooling down to a room temperature, the gas flow was switched to a  $10\% H_2/90\% He$  mixture at 50 mL/min and the temperature was increased to 1000 °C with the ramp of 10 °C/min. The  $H_2$  consumption during reduction was measured by a thermal conductivity detector (TCD). After TPR analysis, the sample was protected in a  $N_2$  gas flow while cooling down to room temperature. Then a  $5\% O_2/95\% Ar$  mixture was applied to the samples at 50 mL/min while the temperature was increased to 1000 °C with the ramp of 10 °C/min. The  $O_2$  consumption during oxidation was also recorded by the TCD.

## 2.5. Gasification of cellulose using the OCs

The gasification of cellulose as a model biomass compound was conducted using the OCs in a Py-GC/MS system that consists of a twostage pyrolyzer (Rx-3050TR, Frontier) and a gas chromatography equipped with a mass spectrometry detector (7890A GC, 5975C MS, Agilent). The pyrolyzer has two reactors connected in series vertically: a top reactor for the pyrolysis of cellulose and a bottom reactor packed with excessive amount of oxygen carrier. In a typical run, a tiny basket loaded with 0.5 mg cellulose was dropped into the top reactor, which was preheated to 700 °C. The cellulose was held in the reactor for 20 s for instant pyrolysis into volatiles The He carrier gas at a constant flow rate of 50 mL/min blew the volatiles downward immediately through the OC-packed reactor preheated at 700-900 °C. The products were introduced into the GC/MS for analysis with a split ratio of 50:1. H2 was not able to be detected due to the use of He as the carrier gas in GC/MS. We did not analyze H<sub>2</sub> in this study as we focused on the analysis of the partial oxidation behavior of OCs. The compounds in the volatile products were identified by comparing their mass spectra to those from the National Institute of Standards and Technology (NIST) mass spectral data library. Since it was generally accepted that chromatographic peak areas of a compound given by GC/MS is proportional to its quantity [19,32], the selectivity of a compound was calculated from the percentage of the peak areas.

#### 2.6. Tar decomposition over the reduced OCs

The catalytic performance of the reduced oxygen carrier in tar decomposition was evaluated in a fixed-bed reactor. A total of 0.3 g oxygen carrier was reduced in a flow of 10%H<sub>2</sub>/90%He mixture at 800 °C for 8 h before loading into the reactor. The catalyst was activated in-situ in H2 flow at 700 °C for 2 h and the carrier gas was then switched to N2 at a flow rate of 30 mL/min. Toluene that was used as a model tar model compound was injected into the carrier gas at a flow rate of 4 mL/h. The temperature of the reactor was maintained constantly at 700 °C. The liquid products and unreacted toluene were collected by a cold trap that was connected with the outlet of the reactor. The gas phase exited from the cold trap was introduced directly into an online gas chromatography (7890B, Agilent) for analysis. The product gases including CO2, CO, H2 CH4 and N2 carrier gas were measured by a TCD. The liquid sample from the cold trap was analyzed by a gas chromatography equipped with a mass spectrometry detector (7890A GC, 5975C MS, Agilent).

The toluene conversion is calculated using Eq. (1):

$$X_{toluene} = \frac{m_{toluene, injected} - m_{toluene, unreacted}}{m_{toluene, injected}} \times 100\%$$
(1)

where  $m_{toluene,\,injected}$  is the total mass of the injected toluene and  $m_{toluene,\,unreacted}$  is the mass of the unreacted toluene identified by GC/MS. The selectivity of the products was calculated using the normalized percentage.

## 2.7. $CO_2$ adsorption on the reduced OCs

The reduced OCs obtained at the same condition for tar decomposition test were used for the  $CO_2$  adsorption capacity analysis. The  $CO_2$  adsorption isotherm was measured on the Micrometrics 3Flex. In a typical experiment, about 0.1 g reduced OC was degassed at 300 °C in situ under vacuum for 8 h. Then the temperature was decreased to 30 °C at which the equilibrium capacity from 0 to 1 bar was measured. The  $CO_2$  adsorption isotherms were fitted using the Freundlich-Langmuir model, as given by Equation (2):

$$q_{eq} = \frac{Q_{sat}KP^n}{KP^n + 1} \tag{2}$$

where  $q_{eq}$  is the amount of  $CO_2$  adsorbed on the reduced OC at equilibrium,  $Q_{sat}$  is the  $CO_2$  adsorption capacity of the adsorbent in saturation, P is the equilibrium pressure of  $CO_2$ , K and n are constants related to adsorption temperature. As comparison,  $H_2$  adsorption isotherms was also measured using the same method to evaluate the potentiality of Fe/S-1 for the separation  $CO_2$  from syngas.

## 3. Results and discussion

#### 3.1. Characterization of OCs

Fig. 2 shows the XRD patterns of the OCs. The characteristic peaks of hematite were detected in all OCs. In comparison with the International Center for Diffraction Data (ICDD) reference code: 00-001-1053, the peaks observed at  $24.2^\circ$ ,  $33.3^\circ$ ,  $35.7^\circ$ ,  $41.0^\circ$ ,  $49.5^\circ$ ,  $54.2^\circ$ ,  $57.6^\circ$ ,  $62.3^\circ$ , and  $64.2^\circ$  are attributed to planes (012), (104), (110), (113), (024), (116), (122), (214), and (300), respectively. Therefore, Fe<sub>2</sub>O<sub>3</sub> were present in all OCs. In Fig. 2a, the broad peaks at around  $22.0^\circ$  ranging from  $15^\circ$  to  $30^\circ$  are typical for amorphous silica, which are the coherent scattering arising from the fixed Si-O bond length [33]. In Fig. 2b, all three OCs containing siliclaite-1 with different Fe<sub>2</sub>O<sub>3</sub>

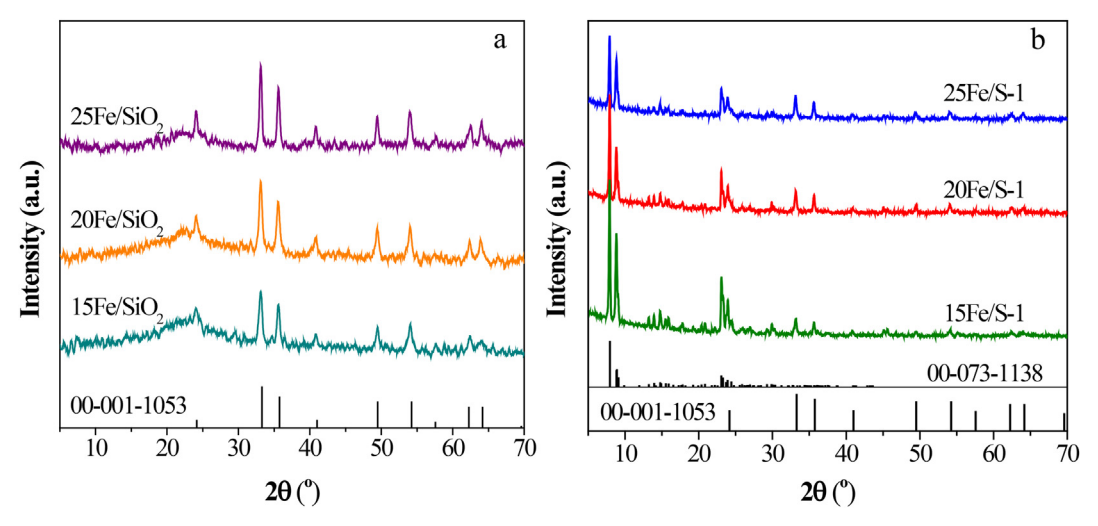


Fig. 2. XRD patterns of the (a) SiO<sub>2</sub>- and (b) silicalite-1-supporting oxygen carriers.

loadings exhibited the patterns for MFI zeolite (ICDD reference code: 01–073-1138), which showed the crystalline nature of the support and the impregnation with iron oxide retained its structure.

Fig. 3 showed the SEM morphology of the OCs. Fig. 3a–c shows all OCs supported on  $SiO_2$  with Fe loadings from 15 to 25% had severe particle agglomerations owing to the impregnation with iron and calcination in the air. The agglomerations were worse in higher Fe-loaded samples because  $Fe_2O_3$  was impregnated on the external surface of the  $SiO_2$  particles, and calcination tended to aggregate the  $Fe_2O_3$  in bulk and thus combine the OC particles. On the other hand, Fe/S-1 samples as shown in Fig. 3d–f exhibited isolated tablet-like particles with uniform size of c.a. 350 nm. Some particles were observed with rough surfaces, as marked in red. These were the  $Fe_2O_3$  formed after calcination from the  $Fe(NO)_3$  solution which failed to enter the pores of the siliclaite-1 and remained at the external surfaces. This is the major limitation of IWI method driven by capillary action [34], as can be proven by the observation that higher Fe loading led to more rough surface ratio.

A closer scrutiny of the  $Fe_2O_3$  supported on silicalite-1, by EDX and element mapping analysis was given in Fig. 4. The EDX spectra shown on the left-hand side in Fig. 4 reveal that the OCs contained Si, O and Fe in accordance with XRD results. The actual Fe loadings calculated from

the area captured by the scattered electron mode (SE) were 13.99, 18.94, and 22.68 wt% for 15Fe/S-1, 20Fe/S-1, and 25Fe/S-1, respectively. Since the intentional loadings were on Fe-basis but the samples contained  $\rm Fe_2O_3$ , it is reasonable that the actual loading was slightly smaller. It is worth mentioning that peaks for carbon, gold, and platinum (out of the displayed range) were also detected. They were attributed to the adhesive material (C) and coating material (Au and Pt) required for the EDX sample preparation, and were neglected in the calculation of the weight percentages of OC elements. The element mappings of Fe (red), O (yellow), and Si (blue) on the right-hand side of Fig. 4 confirmed the uniformity of the siliclaite-1 particles and demonstrated the good dispersion of Fe on the support.

Fig. 5 shows the  $N_2$  adsorption–desorption isotherms. As shown in Fig. 5a,  $SiO_2$ -supporting OCs displayed Type II isotherms which is generally assigned with the physisorption of  $N_2$  on nonporous materials, according to the classification of International Union of Pure and Applied Chemistry (IUPAC) [35]. The shape of constantly increasing curves were the result of unrestricted monolayer-multilayer adsorption up to high  $p/p^\circ$ . Due to the nano-size of the fumed silica particles, demonstrated in Fig. 3a-c, a considerable amount of piled pores was formed [36], leading to a high  $N_2$  uptake at high  $p/p^\circ$  and the Type H3 hysteresis loop. The fact that the surface areas of Fe/SiO<sub>2</sub> samples were

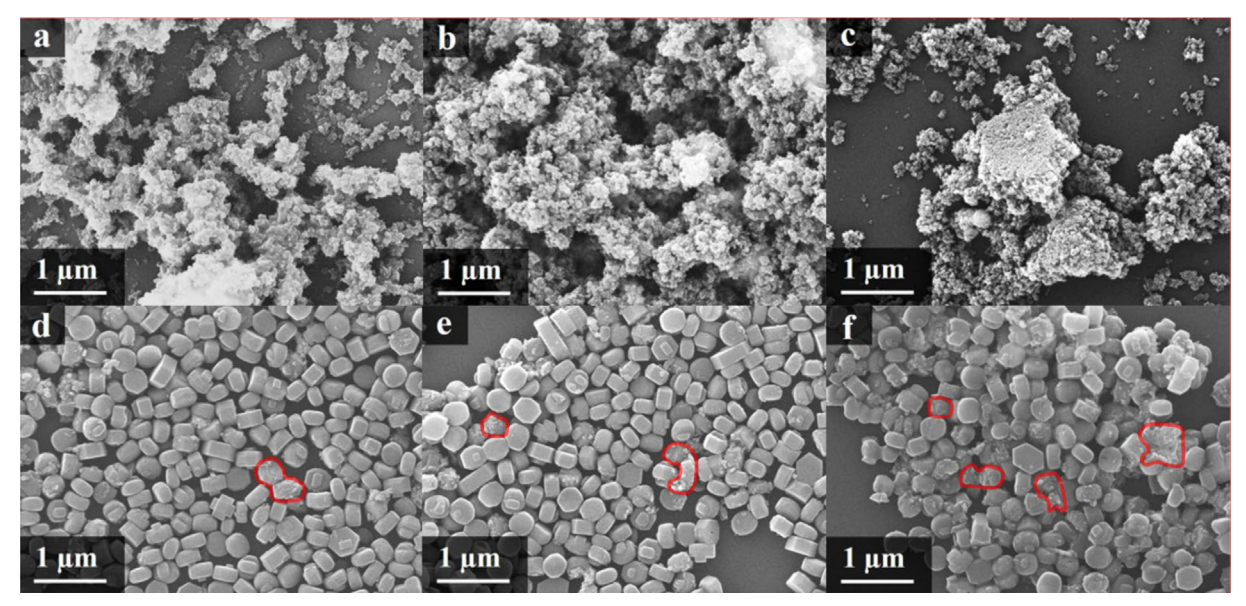


Fig. 3. SEM images of the (a) 15Fe/SiO<sub>2</sub>, (b) 20Fe/SiO<sub>2</sub>, (c) 25Fe/SiO<sub>2</sub>, (d) 15Fe/S-1, (e) 20Fe/S-1, and (f) 25Fe/S-1.

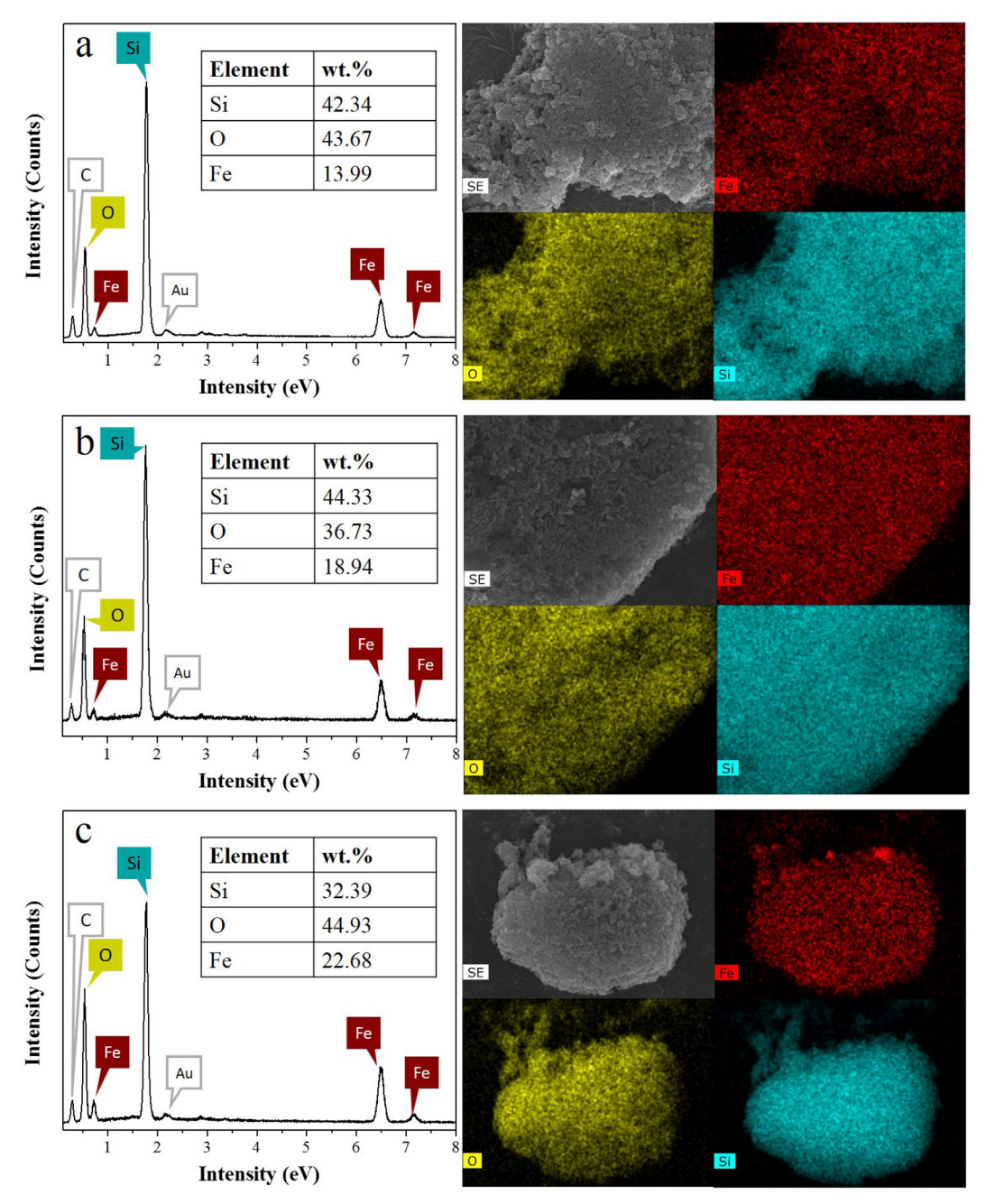


Fig. 4. EDX spectrum (left) and element mapping (right) of (a) 15Fe/S-1, (b) 20Fe/S-1, and (c) 25Fe/S-1.

mainly contributed from external surface areas, as listed in Table 1, also verified their textural properties. The mesopore volume of  $0.92~{\rm cm}^3/{\rm g}$ , mainly given by piled pores, decreased after impregnation with Fe<sub>2</sub>O<sub>3</sub> and because Fe<sub>2</sub>O<sub>3</sub> filled these piled pores. Differently, the isotherms of the OCs with silicalite-1 support, shown in Fig. 5b, displayed a combination of Type I and IV isotherms [37], indicative of microporous nature of siliclaite-1 and the capillary condensation of N<sub>2</sub> in the mesopores, possibly derived from the crystal grain boundaries [38]. Table 1 also showed that the siliclaite-1 support had significant amounts of micropores and mesopores, which contributed surface areas of 228 m²/g and 87 m²/g, respectively. The micropore volume decreased with increasing Fe loading, indicating Fe<sub>2</sub>O<sub>3</sub> entered the micropores upon impregnation.

#### 3.2. Redox behavior of the OCs

Fig. 6 shows the H<sub>2</sub>-TPR and subsequent O<sub>2</sub>-TPO profiles of the oxygen carriers on different supports with various Fe loadings. Comparing the TPR profiles of 15 wt% Fe-supported on silicalite-1 with 15 wt% Fe on SiO<sub>2</sub>, the 15Fe/S-1 profile included three prominent peaks at 333, 472, and 550 °C, which were associated with the reduction of I: hematite (Fe<sub>2</sub>O<sub>3</sub>) to magnetite (Fe<sub>3</sub>O<sub>4</sub>); II: magnetite to wüstite (FeO), and III: wüstite to iron (Fe), respectively [39]. Similarly, the 15Fe/SiO<sub>2</sub> had three peaks at 329, 447, and 562 °C assigned to the same stages. However, a significantly high amount of hydrogen consumption after 650 °C was detected for the 15Fe/SiO<sub>2</sub>, generating a series of peaks at high temperature, as shown by the shaded area in Fig. 6a, in accordance with the findings by Mogorosi et al. [40]. This was mainly caused by the formation of strong Fe–O–Si bonds and various silicate groups during the calcination. The absence of these peaks for 15Fe/S-1

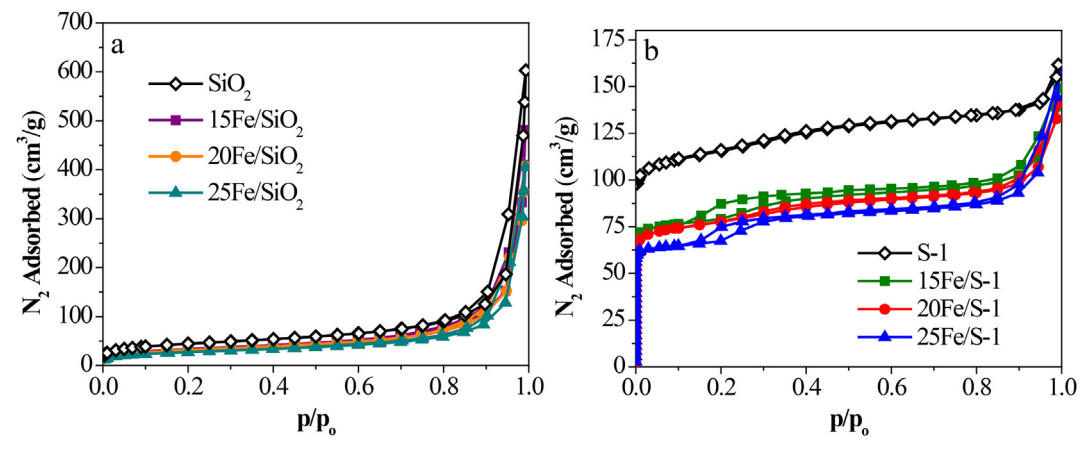


Fig. 5.  $N_2$  adsorption-desorption isotherms of (a) SiO<sub>2</sub>- and (b) silicalite-1-supporting oxygen carriers measured at -196 °C.

Table 1
Surface area and pore volume of the oxygen carriers and corresponding supports.

Sample	$S_{BET}^{a}$ $(m^2/g)$	S <sub>micro</sub> <sup>b</sup> (m <sup>2</sup> /g)	S <sub>ext</sub> <sup>b</sup> (m <sup>2</sup> /g)	V <sub>total</sub> <sup>c</sup> (cm <sup>3</sup> /g)	V <sub>micro</sub> <sup>d</sup> (cm <sup>3</sup> /g)	V <sub>meso</sub> <sup>e</sup> (cm <sup>3</sup> /g)
$SiO_2$	156	27	129	0.93	0.01	0.92
$15$ Fe/SiO $_2$	119	12	107	0.75	_	0.75
20Fe/SiO <sub>2</sub>	112	9	103	0.63	_	0.63
25Fe/SiO <sub>2</sub>	98	12	86	0.63	_	0.63
S-1	315	228	87	0.21	0.11	0.10
15Fe/S-1	263	181	82	0.23	0.09	0.14
20Fe/S-1	246	169	77	0.22	0.09	0.13
25Fe/S-1	232	127	105	0.25	0.06	0.19

 $<sup>^{\</sup>rm a}$  Surface areas were calculated using BET method in the p/p° range of 0.05–0.3.

suggested that siliclaite-1 was more stable during calcination and resistant to form strong metal-support interactions, possibly because the Si–O bonds exists in the crystalline framework and mutual restraint gave rise to chemical stability. The same distinctions were also observed in 20 wt% and 25 wt% Fe-loaded OCs on two different supports.

The lower section of Fig. 6a shows the O2-TPO profiles of the

reduced 15Fe/SiO<sub>2</sub> and 15Fe/S-1 obtained from H<sub>2</sub>-TPR processes. 15Fe/SiO<sub>2</sub> exhibited three peaks at 270, 452, and 940 °C. The two peaks at 270 and 452 °C were associated with (i) surface oxidation and (ii) lattice oxidation, respectively [41]. Oxidation process consists of O2 dissociation to produce O and the transport of O into the lattice. At lower temperature, O2 dissociation is the rate-determining step and the consumption of O2 could be detected on the surface of OCs. As for 15Fe/S-1, only one peak was observed at around 417 °C, which was lower than the bulk oxidation temperature of 452 °C for 15Fe/SiO<sub>2</sub>. This could be caused by the good dispersion of Fe on the siliclaite-1 support requiring less energy to be oxidized, and the high stability of the siliclaite-1 support and thus high resistance to agglomerations and sintering during the reduction stage. The peak at a higher temperature confirmed the formation of strong metal-support interaction and irreversible compounds. Similar profiles were also found in Fig. 6b and c, indicating the redox behavior were independent on Fe loading.

Fig. 7 showed the TPR and TPO profiles of  $15 Fe/SiO_2$  and 15 Fe/S-1 for another two redox cycles. As shown in Fig. 7a, the major reduction temperatures of  $15 Fe/SiO_2$  in the 2nd and 3rd cycles were dramatically increased to nearly 700 °C, compared to 562 °C for the 1st cycle. The shapes of the TPR profiles varied from the 1st cycle. The TPO profile of  $15 Fe/SiO_2$  also exhibited a fluctuating reduction temperature and decreased  $O_2$  consumption in Cycle 3. This further confirmed the formation of strong metal-support interaction and unexpected compounds, as explained before. On the other hand, both TPR and TPO profiles of 15 Fe/S-1 in the 2nd and 3rd cycles as shown in Fig. 7b remained comparable to those obtained in the 1st cycle. The reduction

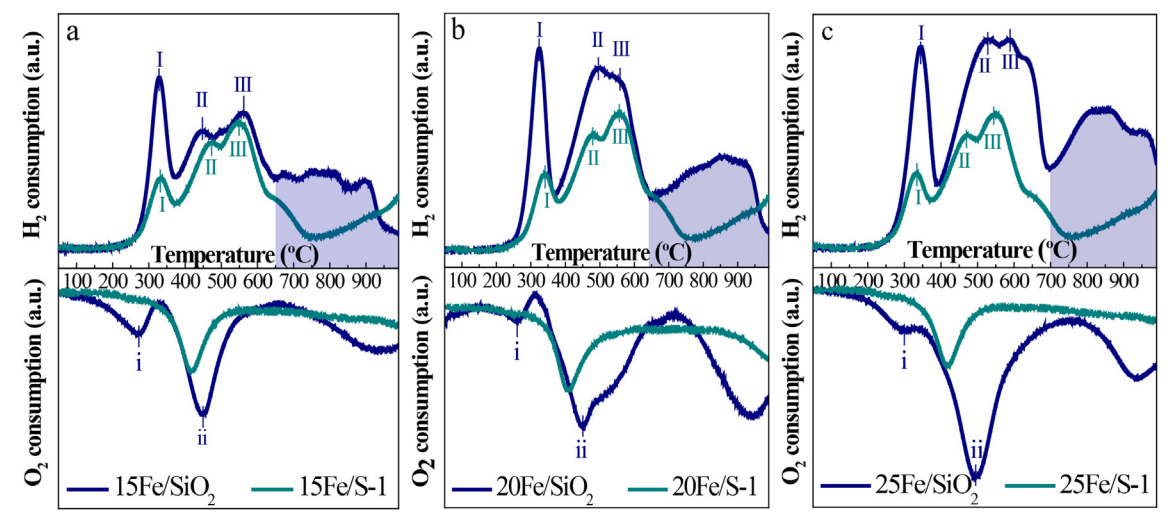


Fig. 6. H<sub>2</sub>-TPR (upper) and O<sub>2</sub>-TPO (lower) profiles of oxygen carriers on different supports with various Fe loadings.

<sup>&</sup>lt;sup>b</sup> Micropore and external surface areas were estimated by t-plot method.

 $<sup>^{</sup>c}$  Total pore volumes were measured from the adsorbed amount at p/  $\vec{p}\,^{\circ}=0.99.$ 

 $<sup>^{\</sup>mathrm{d}}$  Micropore volumes were estimated by t-plot method.

 $V_{\text{meso}} = V_{\text{total}} - V_{\text{micro}}$ 

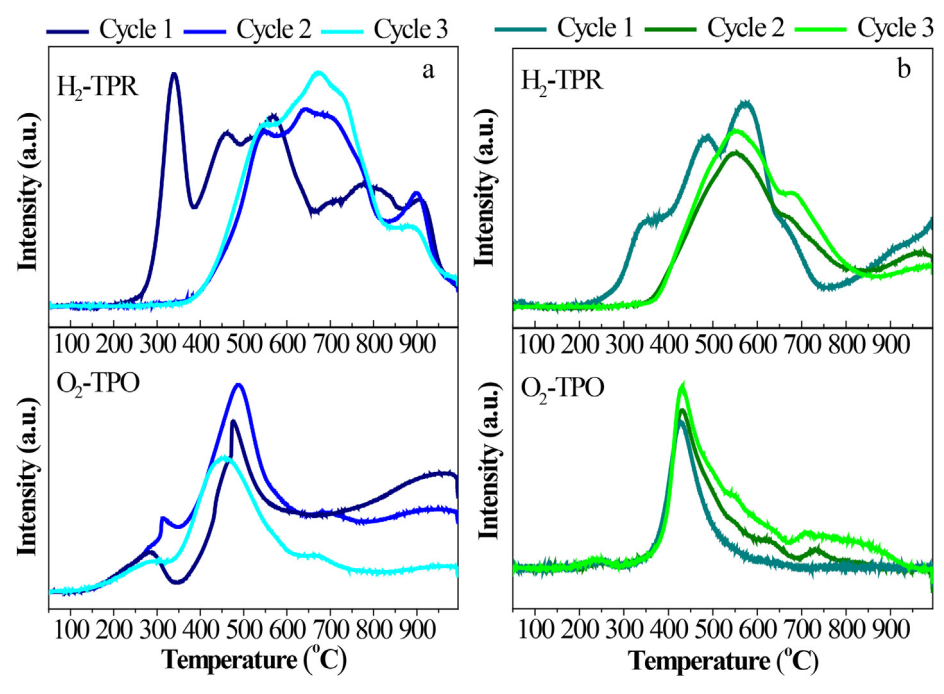


Fig. 7. Cyclic H<sub>2</sub>-TPR (upper) and O<sub>2</sub>-TPO (lower) of (a) 15Fe/SiO2 and (b) 15Fe/S-1.

temperature to form metallic iron retained at around 550  $^{\circ}$ C in TPR while the oxidation temperature to form iron oxide retained at around 430  $^{\circ}$ C. This showed the thermal and chemical stability of the OCs supported on siliclaite-1.

## 3.3. Partial oxidation of cellulose

Fig. 8a illustrates the effect of support type on the product distribution during gasification of cellulose at 900 °C. More  $\rm CO_2$  and  $\rm H_2O$  were identified in the product gases obtained by gasification of cellulose over 15Fe/S-1 than 15Fe/SiO<sub>2</sub> suggested that  $\rm Fe_2O_3$  transferred oxygen more readily when it was loaded on silicalite-1. The good dispersion of  $\rm Fe_2O_3$  and high surface area of silicalite-1 for improved mass transfer facilitated the better oxidation of cellulose over 15Fe/S-1, which matches the  $\rm O_2$ -TPO results. Since the oxidation temperature at 900 °C was high enough to convert most hydrocarbons to  $\rm CO$  and  $\rm CO_2$  [42], no light hydrocarbons at significant amounts were detected. It is noteworthy that the product gas obtained from the gasification of cellulose over 15Fe/S-1 contained 2.9% benzene, which was lower than 3.5% for the use of 15Fe/SiO<sub>2</sub>. Therefore, the 15Fe/S-1 had a potential to produce less tar as benzene has been identified as one of the main

precursors of tar [43]. Fig. 8b shows the product distributions with increasing Fe loading on the silicalite-1 support. The CO<sub>2</sub>/CO ratio obtained by the gasification of cellulose at 900 °C over 15Fe/S-1, 20Fe/ S-1 and 25Fe/S-1 were 2.92, 3.32, and 3.74, respectively. The increase of CO2/CO ratio with the increase of Fe loading on the silicalite-1 support was because more Fe<sub>2</sub>O<sub>3</sub> present in the OC produced more CO<sub>2</sub> and water under the same operating condition. Since it is desirable to have less CO<sub>2</sub> in the syngas, the 15Fe/S-1 was more suitable to be used as an oxygen carrier for the BCLG. Fig. 8c shows the product distribution varied with increasing temperature. At 700 °C, certain C<sub>1</sub>-C<sub>4</sub> hydrocarbons/oxygenates, such as propane, formaldehyde, 2-propenal and furan, were identified. These were the pyrolysis products from the first stage of pyrolyzer [44], which were not oxidized by the lattice oxygen in the second stage. By increasing the temperature from 700 to 900 °C, the amount of these C<sub>1</sub>-C<sub>4</sub> hydrocarbons/oxygenates in the syngas declined from 15.7% at 700 °C to 3.7% at 800 °C and further to 0.6% at 900 °C, while the overall percentages of CO2 and CO increased from 52.1% at 700 °C, to 69.9% at 800 °C and further to 77.0% at 900 °C. As CO<sub>2</sub>/CO ratio change is subtle, namely 2.81, 2.94 and 2.93 under the increasing temperatures, The production of CO was maximized with a selectivity of 19.6% at 900 °C.

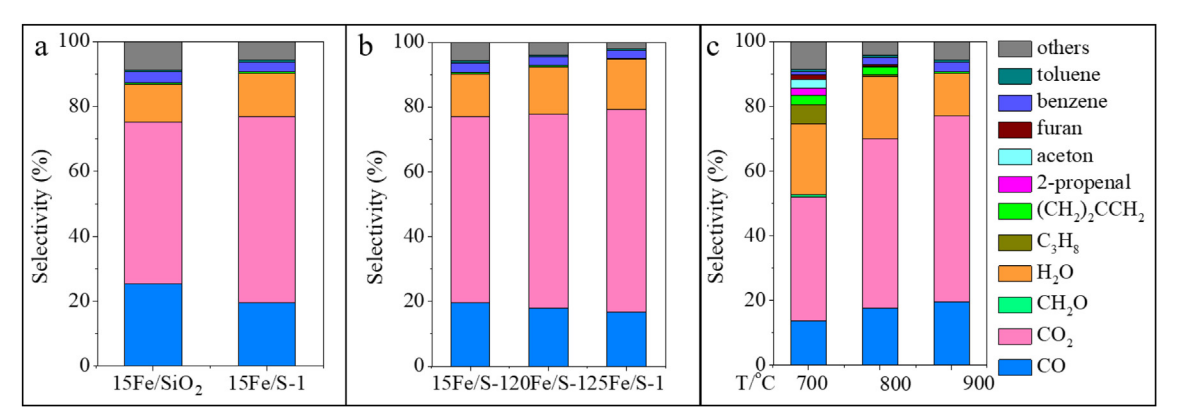


Fig. 8. (a) Product distribution of cellulose gasification over iron oxide on different supports at 900 °C; (b) Product distribution of cellulose gasification over oxygen carriers with various Fe loadings supported on silicalite-1 900 °C; (c) Product distribution of cellulose gasification over 15Fe/S-1 at various temperatures.

 $\begin{tabular}{ll} \textbf{Table 2} \\ \textbf{Catalytic toluene cracking performance of the reduce oxygen carriers with 15\%} \\ \textbf{Fe} \\ \end{tabular}$ 

Reduced OC	X <sub>toluene</sub> (%)	Gas product selectivity (%)		
		H <sub>2</sub>	CH <sub>4</sub>	
15Fe/SiO <sub>2</sub>	23.6	95.3	4.7	
15Fe/S-1	34.8	89.4	10.6	

#### 3.4. Catalytic tar decomposition test

The tar decomposition tests were performed at 700  $^{\circ}$ C in a  $N_2$  flow using toluene as a model compound and the reduced oxygen carriers from the gasifier as the catalyst. Unlike catalytic cracking of tar over an iron oxide-containing catalyst [45], or with co-feeds like steam and  $CO_2$  [46], the reactions for toluene cracking over metallic iron were much simpler and the main reaction is:

$$C_7H_8 \stackrel{catalyst}{\rightarrow} coke + H_2 + CH_4$$

Without an oxygen agent, only H2 and CH4 were identified in the gas products. The conversion of toluene over 15Fe/SiO2 and 15Fe/S-1 at 700 °C were 23.6% and 34.8%, respectively, as shown in Table 2. This showed that silicalite-1 was a promising support not only for an Febased oxygen carrier as discussed in the above section but also for an Fe-based catalyst for tar decomposition. The higher conversion of tar over 15Fe/S-1 was due to the well-dispersed active iron clusters on the support. Tar decomposition over 15Fe/S-1 produced less H2. The possible reason could be that the silicalite-1 supported iron was more resistant to the formation of coke from tar, which meanwhile reduced the release of hydrogen [47]. The conversion of tars in the syngas can avoid its contamination of catalysts in downstream processes. Although the formation of coke could deactivate a catalyst used for tar decomposition, the coke on the reduced OCs as a catalyst could be easily removed by the further regeneration of the OCs via oxidation in air. It is worthy to note that the chromatographic profiles of the collected liquid after tar decomposition showed traceable amounts of intermediates such as benzene, n-hexane, and methylcyclopentane.

### 3.5. CO2 adsorption over reduced OCs

As the proposed BCLG shown in Fig. 1, the reduced OC was used as an adsorbent for  $CO_2$  capture at a low temperature. Therefore, the  $CO_2$  adsorption isotherms of reduced Fe/S-1 samples at 30 °C were measured and plotted in Fig. 9. As the  $R^2$  values of all the fitting curves generated by the Freundlich-Langmuir model were greater than 0.99, the model was effective to describe the adsorption performance of this

material [48]. At 1 bar, the reduced 15Fe/S-1, 20Fe/S-1 and 25Fe/S-1 had CO<sub>2</sub> adsorption capacity of 1.01, 0.91 and 0.84 mmol/g, respectively. The values of Qsat, which represents the adsorption capacity at saturation, were 2.29, 2.18, and 2.03 mmol/g for 15Fe/S-1, 20Fe/S-1 and 25Fe/S-1, respectively. The comparison between the CO2 adsorption capacity at 1 bar and the adsorption capacity at saturation suggests that CO2 adsorption was not saturated over all three samples at a pressure below 1 bar, which was in accordance with the shapes of the isotherms. The adsorption capacities of these reduced oxygen carriers were comparable to those of many adsorbents used for CO2 adoption reported in literature, for example 1.0 mmol/g of MIL-101 metal-organic framework [49] and 1.10 mmol/g of Na-BEA zeolite [50]. The CO<sub>2</sub> capture capacity was reduced with increasing Fe loading because the impregnation of Fe decreased the surface area and total pore volume of the silicalite-1 support. In consideration of the above-mentioned enhancement of syngas production and the reduction of tar, as well as the higher CO2 uptake over the sample with 15% Fe, it is evident that less Fe loading favors upgrading the syngas. As all samples exhibited a much lower adsorption capacity of H2 than CO2, the Fe/S-1 is a promising material for selective separation of CO<sub>2</sub> from H<sub>2</sub>-containing syngas.

#### 4. Conclusions

The inexpensive and accessible iron oxide supported on silicalie-1 had lower reduction and oxidation temperatures than iron oxide supported on conventional silica. Unlike the conventional amorphous silica, the Si-O bonds of silicalite-1 refrained by the crystalline framework led to a high thermal/chemical stability, giving rise to the resistance to the formation of strong metal-support interaction and irreversible silicates. As a high surface area and microporous channels could well immobilize and disperse the oxide clusters, Fe<sub>2</sub>O<sub>3</sub> supported on silicalite-1 transferred oxygen atoms readily in the partial oxidation of cellulose. Lower Fe loading of 15 wt% at 900 °C favored the production of syngas with high contents of valuable gaseous compounds of H2 and CO. The metallic iron on siliclaite-1 outperformed it on conventional silica in toluene catalytic cracking, with a 34.8% conversion and 89.4% hydrogen selectivity, which demonstrated its ability to remove tar from the syngas and generate more hydrogen to enhance the value of the syngas. The outstanding CO<sub>2</sub> adsorption capacity of 1.01 mmol/g CO<sub>2</sub> at 30 °C under 1 bar, originated from the high surface area of silicalite-1 support, was comparable to many CO2 adsorbents. The feasibility of the multifunctional material as the oxygen carrier for biomass chemical looping gasification is verified. Future work will be focused on the applications of the novel OC in the gasification of real biomass, catalytic cracking of biotar in syngas, and the performance of reduced OC mixed with biochar, which is an inevitable byproduct in gasification. The

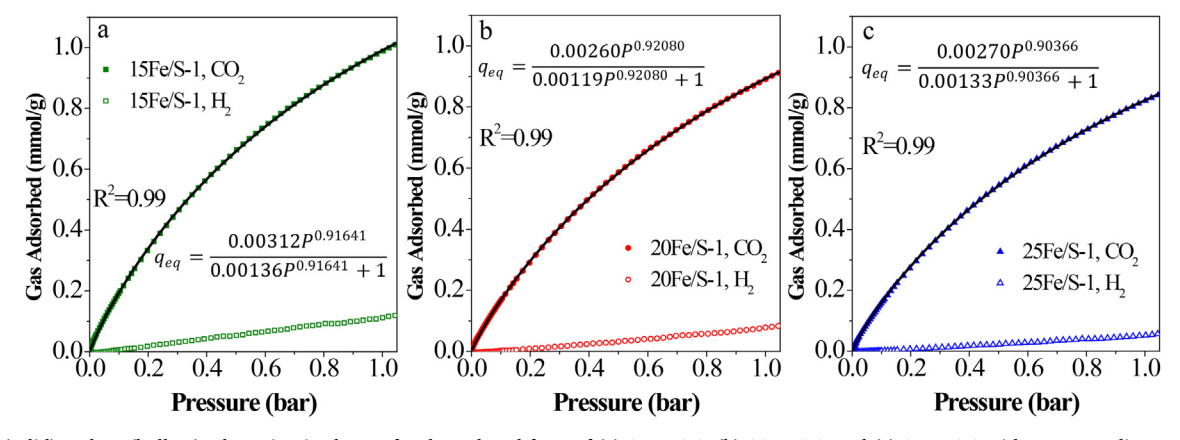


Fig. 9. CO<sub>2</sub> (solid) and H<sub>2</sub> (hollow) adsorption isotherms for the reduced form of (a) 15Fe/S-1, (b) 20Fe/S-1, and (c) 15Fe/S-1 with corresponding equation of the fitting curve using the Freundlich-Langmuir model.

cyclic tests of the novel OC with more cycles will also be included in the future work to examine the performance of the thermal/chemical stability.

#### **Declaration of Competing Interest**

The authors declare that they have no known competing financial interests or personal relationships that could have appeared to influence the work reported in this paper.

#### Acknowledgements

A contribution of North Carolina Agricultural and Technical State University, supported by funds provided by U.S National Science Foundation (Grant #: HRD-1736173). Mention of a trade name, proprietary products, or company name is for presentation clarity and does not imply endorsement by the authors or the university.

#### References

- P. McKendry, Energy production from biomass (part 2): conversion technologies, Bioresour. Technol. 83 (2002) 47–54.
- [2] X. Zhao, H. Zhou, V.S. Sikarwar, M. Zhao, A.-H.A. Park, P.S. Fennell, L. Shen, L.-S. Fan, Biomass-based chemical looping technologies: the good, the bad and the future, Energy Environ. Sci. 10 (2017) 1885–1910.
- [3] N. Kobayashi, L.-S. Fan, Biomass direct chemical looping process: A perspective, Biomass Bioenergy 35 (2011) 1252–1262.
- [4] J. Han, H. Kim, The reduction and control technology of tar during biomass gasification/pyrolysis: An overview, Renew. Sustain. Energy Rev. 12 (2008) 397–416.
- [5] B. Moghtaderi, Review of the recent chemical looping process developments for novel energy and fuel applications, Energy Fuels 26 (2012) 15–40.
- [6] L.-S. Fan, L. Zeng, S. Luo, Chemical-looping technology platform, 61 (2015) 2-22.
- [7] S. Luo, L. Zeng, L.-S. Fan, Chemical Looping Technology: Oxygen Carrier Characteristics, 6 (2015) 53-75.
- [8] H. Ge, W. Guo, L. Shen, T. Song, J. Xiao, Biomass gasification using chemical looping in a 25kWth reactor with natural hematite as oxygen carrier, Chem. Eng. J. 286 (2016) 174–183.
- [9] C. Wu, L. Wang, P.T. Williams, J. Shi, J. Huang, Hydrogen production from biomass gasification with Ni/MCM-41 catalysts: Influence of Ni content, Appl. Catal. B: Environ. 108-109 (2011) 6–13.
- [10] P. Cho, T. Mattisson, A. Lyngfelt, Comparison of iron-, nickel-, copper- and manganese-based oxygen carriers for chemical-looping combustion, Fuel 83 (2004) 1215–1225.
- [11] L. Liu, M.R. Zachariah, Enhanced performance of alkali metal doped Fe2O3 and Fe2O3/Al2O3 composites as oxygen carrier material in chemical looping combustion, Energy Fuels 27 (2013) 4977–4983.
- [12] Q. Imtiaz, N.S. Yüzbasi, P.M. Abdala, A.M. Kierzkowska, W. van Beek, M. Broda, C.R. Müller, Development of MgAl2O4-stabilized, Cu-doped, Fe2O3-based oxygen carriers for thermochemical water-splitting, J. Mater. Chem. A 4 (2016) 113–123.
- [13] S. Ma, M. Li, G. Wang, L. Zhang, S. Chen, Z. Sun, J. Hu, M. Zhu, W. Xiang, Effects of Zr doping on Fe2O3/CeO2 oxygen carrier in chemical looping hydrogen generation, Chem. Eng. J. 346 (2018) 712–725.
- [14] L. Protasova, F. Snijkers, Recent developments in oxygen carrier materials for hydrogen production via chemical looping processes, Fuel 181 (2016) 75–93.
- [15] J. Adánez, L.F. de Diego, F. García-Labiano, P. Gayán, A. Abad, J.M. Palacios, Selection of oxygen carriers for chemical-looping combustion, Energy Fuels 18 (2004) 371–377.
- [16] A. Abad, J. Adánez, F. García-Labiano, L.F. de Diego, P. Gayán, J. Celaya, Mapping of the range of operational conditions for Cu-, Fe-, and Ni-based oxygen carriers in chemical-looping combustion, Chem. Eng. Sci. 62 (2007) 533–549.
- [17] S.S. Tamhankar, K. Tsuchiya, J.B. Riggs, Catalytic cracking of benzene on iron oxide-silica: catalyst activity and reaction mechanism, Appl. Catal. 16 (1985) 102, 121
- [18] X.-Y. Zhao, J. Ren, J.-P. Cao, F. Wei, C. Zhu, X. Fan, Y.-P. Zhao, X.-Y. Wei, Catalytic reforming of volatiles from biomass pyrolysis for hydrogen-rich gas production over limonite ore, Energy Fuels 31 (2017) 4054–4060.
- [19] L. He, H. Hui, S. Li, W. Lin, Production of light aromatic hydrocarbons by catalytic cracking of coal pyrolysis vapors over natural iron ores, Fuel 216 (2018) 227–232.
- [20] T. Nordgreen, T. Liliedahl, K. Sjöström, Metallic iron as a tar breakdown catalyst related to atmospheric, fluidised bed gasification of biomass, Fuel 85 (2006) 689–694.
- [21] E. Jerndal, T. Mattisson, A. Lyngfelt, Thermal analysis of chemical-looping combustion, Chem. Eng. Res. Des. 84 (2006) 795–806.
- [22] P. Munnik, P.E. de Jongh, K.P. de Jong, Control and impact of the nanoscale distribution of supported cobalt particles used in fischer-tropsch catalysis, J. Am. Chem. Soc. 136 (2014) 7333–7340.
- [23] T.M. Eggenhuisen, J.P.D. Breejen, D. Verdoes, P.E.D. Jongh, K.P.D. Jong,

- Fundamentals of Melt infiltration for the preparation of supported metal catalysts. The case of Co/SiO2 for Fischer Tropsch synthesis, J. Am. Chem. Soc. 132 (2010) 18318–18325.
- [24] S. Sun, M. Zhao, L. Cai, S. Zhang, D. Zeng, R. Xiao, Performance of CeO2-modified iron-based oxygen carrier in the chemical looping hydrogen generation process, Energy Fuels 29 (2015) 7612–7621.
- [25] X. Zheng, Q. Su, W. Mi, P. Zhang, Effect of steam reforming on methane-fueled chemical looping combustion with Cu-based oxygen carrier, Int. J. Hydrogen Energy 39 (2014) 9158–9168.
- [26] S.K. Wirawan, D. Creaser, J. Lindmark, J. Hedlund, I.M. Bendiyasa, W.B. Sediawan, H2/CO2 permeation through a silicalite-1 composite membrane, J. Membr. Sci. 375 (2011) 313–322.
- [27] S.K. Wirawan, D. Creaser, CO2 adsorption on silicalite-1 and cation exchanged ZSM-5 zeolites using a step change response method, Microporous Mesoporous Mater. 91 (2006) 196–205.
- [28] J.J. Lara-Medina, M. Torres-Rodríguez, M. Gutiérrez-Arzaluz, V. Mugica-Alvarez, Separation of CO2 and N2 with a lithium-modified silicalite-1 zeolite membrane, Int. J. Greenhouse Gas Control 10 (2012) 494–500.
- [29] N. Wang, Q. Sun, R. Bai, X. Li, G. Guo, J. Yu, In situ confinement of ultrasmall Pd Clusters within nanosized silicalite-1 zeolite for highly efficient catalysis of hydrogen generation, J. Am. Chem. Soc. 138 (2016) 7484–7487.
- [30] L. Shi, G. Liu, H. Guo, Efficient Pt/Silicalite-1 catalyst for isomerization of n-heptane, Catal. Commun. 101 (2017) 111–115.
- [31] P. Arudra, T.I. Bhuiyan, M.N. Akhtar, A.M. Aitani, S.S. Al-Khattaf, H. Hattori, Silicalite-1 as efficient catalyst for production of propene from 1-butene, ACS Catal. 4 (2014) 4205–4214.
- [32] Q. Lu, Y. Zhang, Z. Tang, W.-Z. Li, X.-F. Zhu, Catalytic upgrading of biomass fast pyrolysis vapors with titania and zirconia/titania based catalysts, Fuel 89 (2010) 2096–2103.
- [33] Q. Mei, C.J. Benmore, S. Sen, R. Sharma, J.L. Yarger, Intermediate range order in vitreous silica from a partial structure factor analysis, Phys. Rev. B 78 (2008) 144204.
- [34] X. Sun, A.I.O. Suarez, M. Meijerink, T. van Deelen, S. Ould-Chikh, J. Zečević, K.P. de Jong, F. Kapteijn, J. Gascon, Manufacture of highly loaded silica-supported cobalt Fischer-Tropsch catalysts from a metal organic framework, Nat. Commun. 8 (2017) 1680.
- [35] M. Thommes, K. Kaneko, A.V. Neimark, J.P. Olivier, F. Rodriguez-Reinoso, J. Rouquerol, K.S.J.P. Sing, A. Chemistry, Physisorption of gases, with special reference to the evaluation of surface area and pore size distribution, (IUPAC Technical Report) 87 (2015) 1051–1069.
- [36] Y. Wang, B. Chen, Y. Zhang, L. Fu, Y. Zhu, L. Zhang, Y.J.E.A. Wu, ZIF-8@ MWCNT-derived carbon composite as electrode of high performance for supercapacitor, 213 (2016) 260-269.
- [37] W. Panpa, S. Jinawath, Synthesis of ZSM-5 zeolite and silicalite from rice husk ash, Appl. Catal. B 90 (2009) 389–394.
- [38] J. Choi, H.-K. Jeong, M.A. Snyder, J.A. Stoeger, R.I. Masel, M.J.S. Tsapatsis, Grain boundary defect elimination in a zeolite membrane by rapid thermal processing, 325 (2009) 590-593.
- [39] W.K. Jozwiak, E. Kaczmarek, T.P. Maniecki, W. Ignaczak, W. Maniukiewicz, Reduction behavior of iron oxides in hydrogen and carbon monoxide atmospheres, Appl. Catal. A 326 (2007) 17–27.
- [40] R.P. Mogorosi, N. Fischer, M. Claeys, E. van Steen, Strong-metal-support interaction by molecular design: Fe-silicate interactions in Fischer-Tropsch catalysts, J. Catal. 289 (2012) 140–150.
- [41] T.-J. Huang, X.-D. Shen, C.-L. Chou, Characterization of Cu, Ag and Pt added La0.6Sr0.4Co0.2Fe0.8O3 – δ and gadolinia-doped ceria as solid oxide fuel cell electrodes by temperature-programmed techniques, J. Power Sources 187 (2009) 348–355.
- [42] K.C. Stein, J.J. Feenan, G.P. Thompson, J.F. Shultz, L.J.E. Hofer, R.B. Anderson, The oxidation of hydrocarbons on simple oxide catalysts, J. Air Pollut. Control Assoc. 10 (1960) 275–281.
- [43] T.A. Milne, R.J. Evans, N. Abatzaglou, Biomass gasifier "Tars": their nature, formation, and conversion, National Renewable Energy Laboratory, Golden, CO (US), 1998.
- [44] J. Yu, N. Paterson, M. Millan, The primary products of cellulose pyrolysis in the absence of extraparticle reactions, Fuel 237 (2019) 911–915.
- [45] X. Zou, T. Chen, H. Liu, P. Zhang, D. Chen, C. Zhu, Catalytic cracking of toluene over hematite derived from thermally treated natural limonite, Fuel 177 (2016) 180–189.
- [46] S. Kang, M. He, C. Yin, H. Xu, Q. Cai, Y. Wang, L. Cui, Graphitic carbon embedded with Fe/Ni nano-catalysts derived from bacterial precursor for efficient toluene cracking, Green Chem. (2020).
- [47] W.G. Appleby, J.W. Gibson, G.M. Good, Coke formation in catalytic cracking, Ind. Eng. Chem. Process Des. Dev. 1 (1962) 102–110.
- [48] S. Lawson, B. Adebayo, C. Robinson, Q. Al-Naddaf, A.A. Rownaghi, F. Rezaei, The effects of cell density and intrinsic porosity on structural properties and adsorption kinetics in 3D-printed zeolite monoliths, Chem. Eng. Sci. 218 (2020) 115564.
- [49] S. Lawson, C. Griffin, K. Rapp, A.A. Rownaghi, F.J.E. Rezaei, fuels, Amine-functionalized MIL-101 monoliths for CO2 removal from enclosed environments, 33 (2019) 2399-2407.
- [50] S.-T. Yang, J. Kim, W.-S. Ahn, CO2 adsorption over ion-exchanged zeolite beta with alkali and alkaline earth metal ions, Microporous Mesoporous Mater. 135 (2010) 90–94